

Supporting Information

Ultrahigh Sensitivity Micro-cliff Graphene Wearable Pressure Sensor Made by Instant Flash Light Exposure

Yachu Zhang, Han Lin, Fei Meng, Huai Liu, David Mesa, Huihui Zhang, Xiaodong Huang, Alan Kin Tak Lau, Yuejin Zhao*, Tianyi Ma*, Baohua Jia**

Y. C. Zhang, Dr. H. Lin, Dr. F. Meng, H. H. Zhang, Prof. X. D. Huang, Prof. A. K. T. Lau, Prof. T. Y. Ma, Prof. B. H. Jia

Centre for Translational Atomaterials, Faculty of Science, Engineering and Technology, Swinburne University of Technology

P. O .Box 218, Hawthorn VIC 3122, Australia

E-mail: hanlin@swin.edu.au; tianyima@swin.edu.au; bjia@swin.edu.au

Dr. H. Liu

Department of Computer Science and Software Engineering, Swinburne University of Technology

P. O .Box 218, Hawthorn VIC 3122, Australia

D. Mesa

Faculty of Health Arts and Design, Swinburne University of Technology

P. O .Box 218, Hawthorn VIC 3122, Australia

Prof. Y. J. Zhao

Beijing Key Laboratory for Precision Optoelectronic Measurement Instrument and Technology, School of Optics and Photonics, Beijing Institute of Technology

Beijing 100081, China

E-mail: yjzhao@bit.edu.cn

1. Simulation of the piezoresistive principle of micro-cliff structure

The model parameters of the micro-cliff were set according to the cross-sectional SEM images and microscope images, which has shown in the **Figure 2**, and the modeling graphic in software is shown in **Figure S1a**. The load was controlled to apply on the micro-cliff structure, representing in the increased load displacement (**Figure S1b**). The Young's modulus and Possion ratio are set as 7 GPa and 0.272, respectively, which have the same order of magnitude refer to the references.^{[1][2][3]} To be noted, the Young's modulus and Possion ratio value here is an estimated value, because the overall Young's modulus and Possion ratio also depend on the structure of the material, which may vary from the one measured from the flat 2D material in the references.

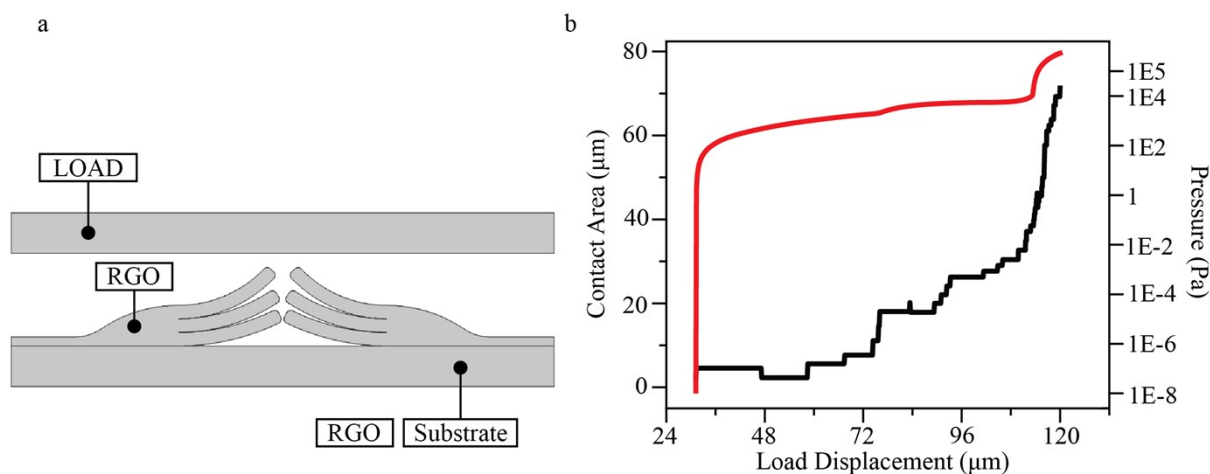


Figure S1. Simulation model and result (a) Simulation model (b) Simulation result of relationship between contact area, pressure and load displacement

2. X-ray photoelectron spectroscopy (XPS) results, Raman spectral results, and conductivity of RGO film

The XPS analysis of GO films before and after reduction are shown in **Figure S2**. After reduction, the C:O ratio has been significantly increased from 3.38 of GO film to 11.47 of RGO film (**Figure S2a**), which demonstrates the effective dissociation of oxygen-containing functional groups (OCFGs) after flash reduction of GO films. **Figure S2b** and **Figure S2c** shows the XPS analysis for C1s peak of GO and RGO samples. For GO films, the OCFGs are mainly C-O, C=O and C=O-OH bonds. The above OCFGs have been effectively removed after flash reduction process, as the dominant C-C peak up to 70 at% is identified in **Figure S2c**. This suggests the restoration of C-C sp² structure after flash reduction. Both high C:O ratio in wide scan survey and dominant C-C bonding in C1s peak indicate the synthesis of high-quality RGO material after flash reduction.

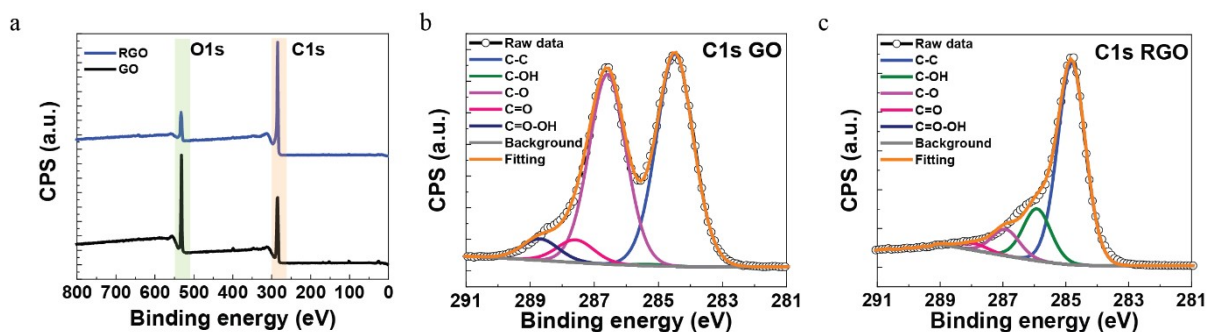


Figure S2. X-ray photoelectron spectroscopy (XPS) results. (a) XPS survey analysis for GO and RGO films (b) XPS analysis of C1s peaks for GO films (c) XPS analysis of C1s peaks for RGO films

Figure S3 shows the Raman spectra for GO and RGO. GO sample exhibits both strong D and G band located at 1372 cm^{-1} and 1602 cm^{-1} , respectively. The red shift in both D and G band compared to pristine graphene suggests the attachment of OCFGs to the graphene network. After flash reduction, the D band shifts to around 1354 cm^{-1} and the G band is identified at around 1595 cm^{-1} . The blue shift in D and G band after flash reduction demonstrates the removal of OCFGs and the restoration of graphitic sp^2 structure. The effective reduction of GO has also been indicated by the decrease in I_D/I_G ratio from 1.11 to 1.09 after reduction. It is noted that the D band still shows high intensity after flash reduction, suggests high density of structural defects such as pores and cracks in RGO films. Evidence of 2D peak is also shown in **Figure S2**, suggesting the formation of high quality graphene networks.

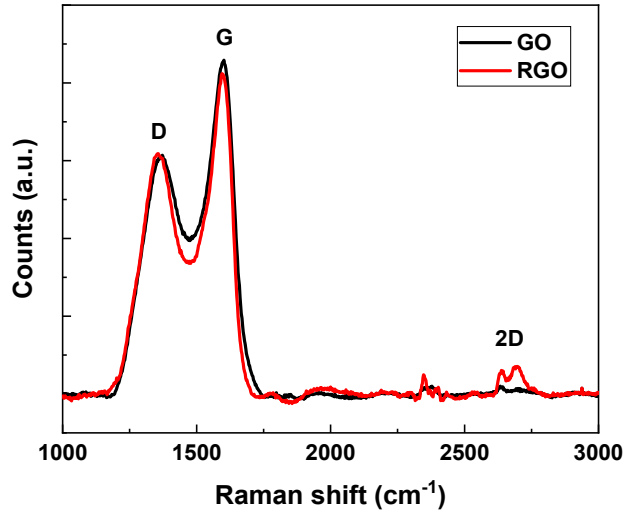


Figure S3. Raman spectra for GO and RGO.

Besides, the electrical conductivity of RGO film is measured through multimeter, which is 52 ± 10 S/m.

3. Micro-cliff structural deformation along with the pressure applied

Our micro-cliff structure deforms when pressure is applied. The contact area increases as pressure is applied hence increasing the conductivity and decreasing the resistance. To visually illustrate the contact progress, the effect of applied pressure on micro-cliff structural deformation along with the applied pressure is characterized using an optical microscope, as shown in **Figure S4**.

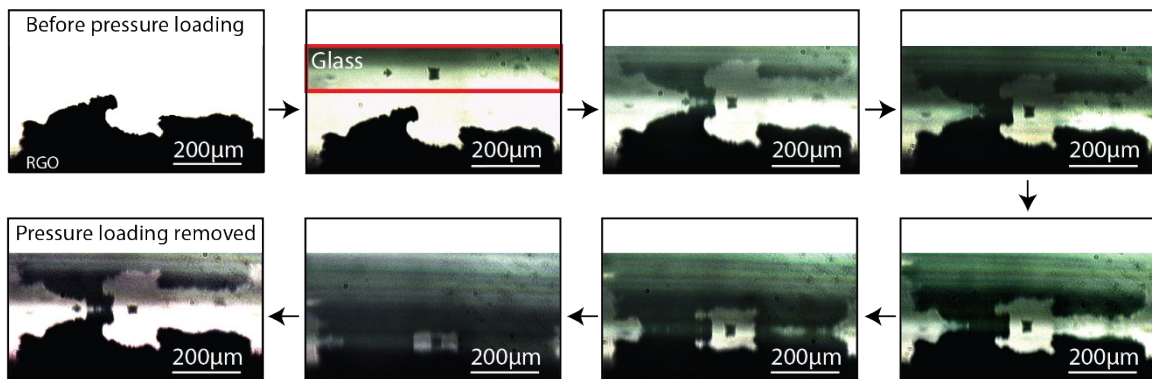


Figure S4. Micro-cliff graphene sensor deformation process. The images following the arrow direction show the deformation process within soft to hard force pressure loaded and unloaded.

4. Side-view of micro-cliff structure and three-dimensional micro-cliff structure along the depth direction

Figure S5 shows the side-view and top-view scanning electron microscope (SEM) images of micro-cliff structures. As can be seen in side-view images **Figure S5 (a)** and **(b)**, it is hard to observe clear structures owing to the irregular cut edges and its deep structures. Due to the low conductivity of the GO film, we can see strong charging effect which shows in the white area. Instead, using optical microscope, the images (**Figure S6**) of the micro-cliff structure have been taken at different depths. The deformation process occurred in different depths of the structure and caused uneven contact at different “cliffs”. **Figure S5 (c)** shows the surface nanostructure of the RGO film.

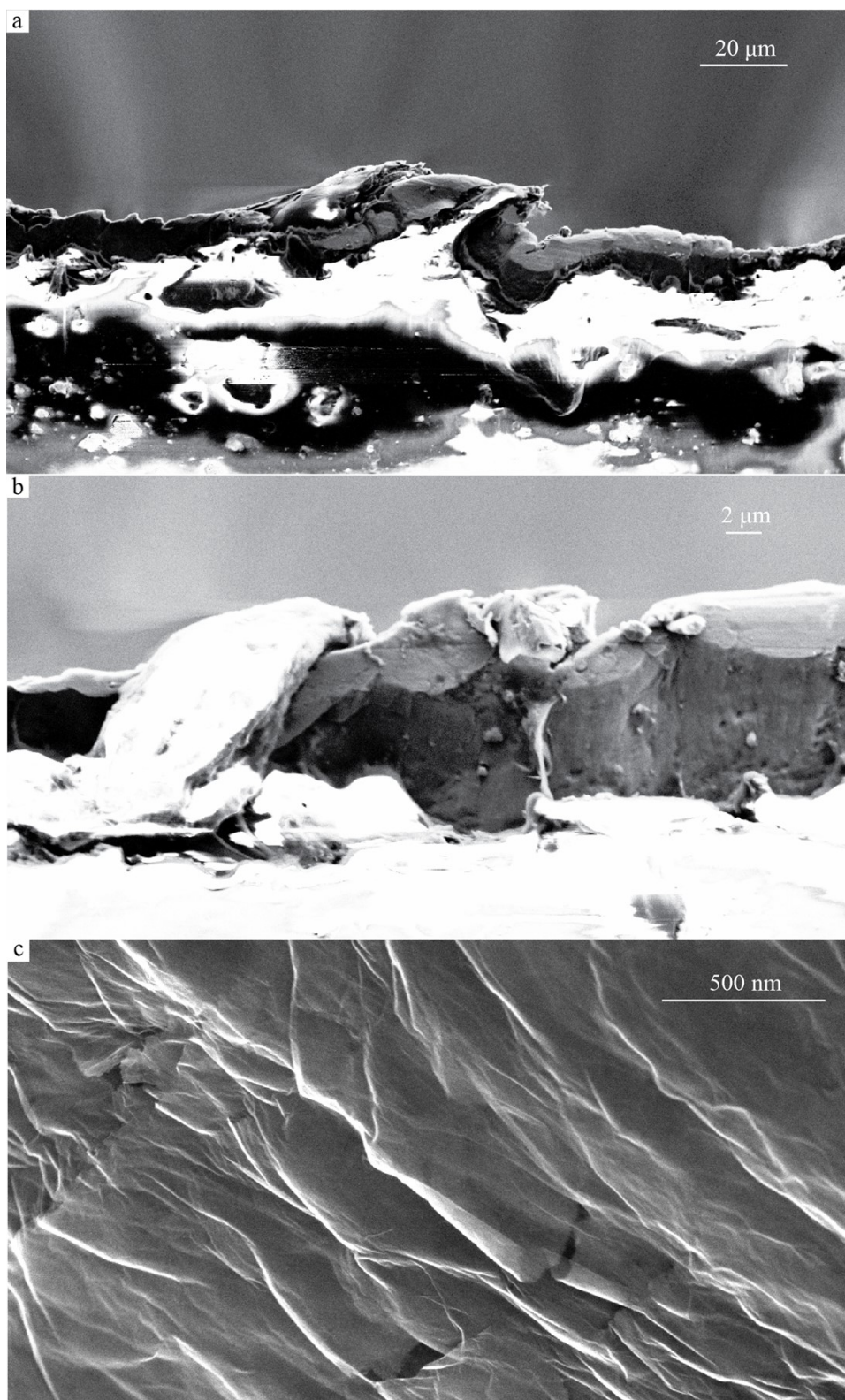


Figure S5. SEM images of the side-view and top-view of the micro-cliff structure. (a) and (b) are SEM images of the side-view with 2000× and 8000× magnification, respectively. (c) Top-view SEM image of surface nanostructure of the RGO film.

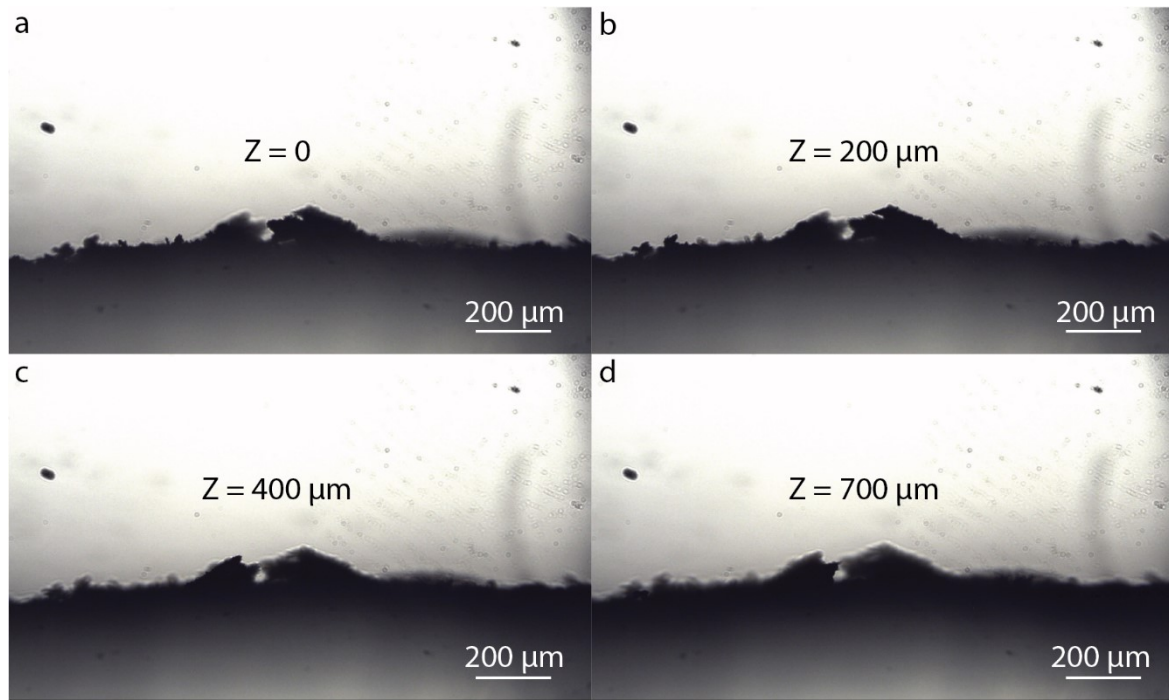


Figure S6. Three-dimensional micro-cliff structure of the RGO sensor. (a) to (d) are three-dimensional structures of the micro-cliff along the depth direction with different focal positions. If we define the depth (z) of the clear part of (a) is $z = 0$, then the depth of clear parts in (b), (c) and (d) are $200 \mu m$, $400 \mu m$, $700 \mu m$, respectively.

5. Sensor performance measuring circuit

The sensor performance measuring circuit consists of 4 parts: DC supply, oscilloscope, $10k\Omega$ resistor, and sensor. The DC supply provides a voltage of 5V applied in series to a $10k\Omega$ resistor and sensor. In the series circuit, when the resistance of the pressure sensor changes due to the pressure, its voltage value will change and be recorded by the oscilloscope.

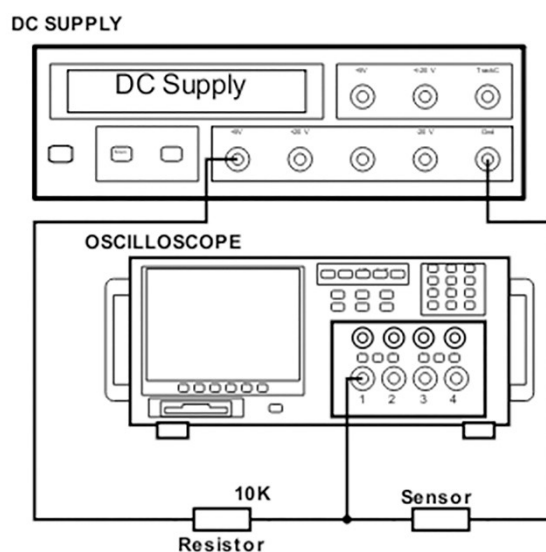
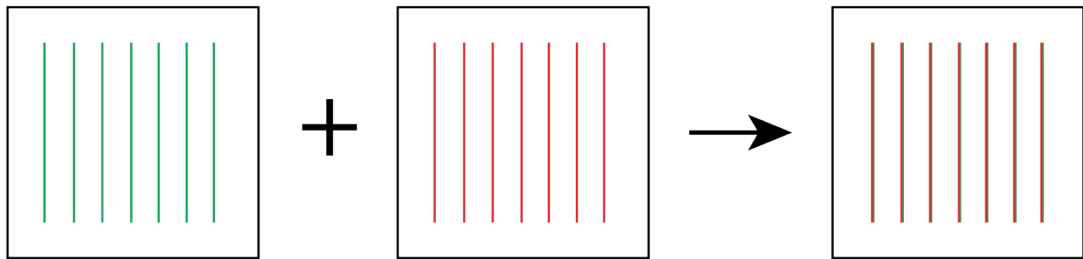


Figure S7. The sensor performance measuring circuit.

6. Different assemble methods for sensors

We used two different assemble methods for the micro-cliff graphene pressure sensor and subsequently compared their performance. The schematics corresponding to these two methods are shown in Figure S8. For the first assemble method (**Figure. S8a**), each RGO line of one sensing layer overlaps the corresponding lines of another layer (may have a small spatial shift). We call the sensor made by this method ‘overlapping pattern sensor’. The second assemble method (**Figure S8b**) is to rotate one layer 90 degrees compared to the prior layer, leading to each RGO line of one layer perpendicular to the RGO lines of the other layer. This kind of sensor is called ‘cross pattern sensor’. To be noted, the overlapping patterned films can benefit both sensitivity and working range (as shown in **Figure 5a**).

a



b

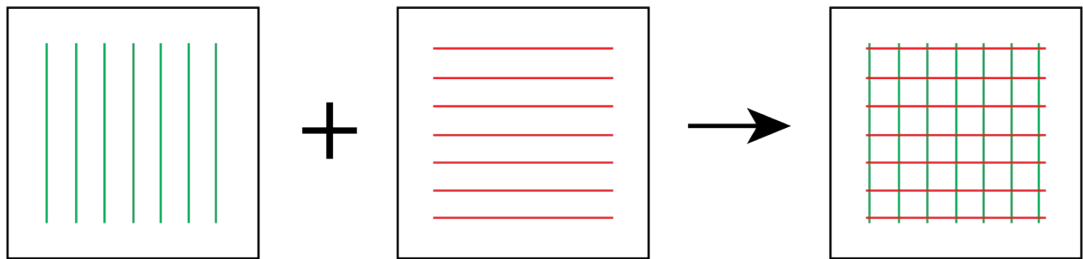


Figure S8. Two kind of pattern sensor using different assemble method (a) overlapping pattern sensor
(b) cross pattern sensor

7. RGO pressure sensor without pattern and its sensing performance

The specified pattern (micro-cliff RGO lines) is the key factor to achieve the ultrahigh sensitivity, because only the RGO lines have the micro-cliff structure. For comparison, here we capture the optical microscopy and SEM images (**Figure S9**) to show the flash-reduced GO sensing layers without the micro-cliff structures. The device without micro-cliff structure shows poor sensitivity (1.125 kPa^{-1}) and small working range (0-14 kPa) as shown in **Figure S10**.

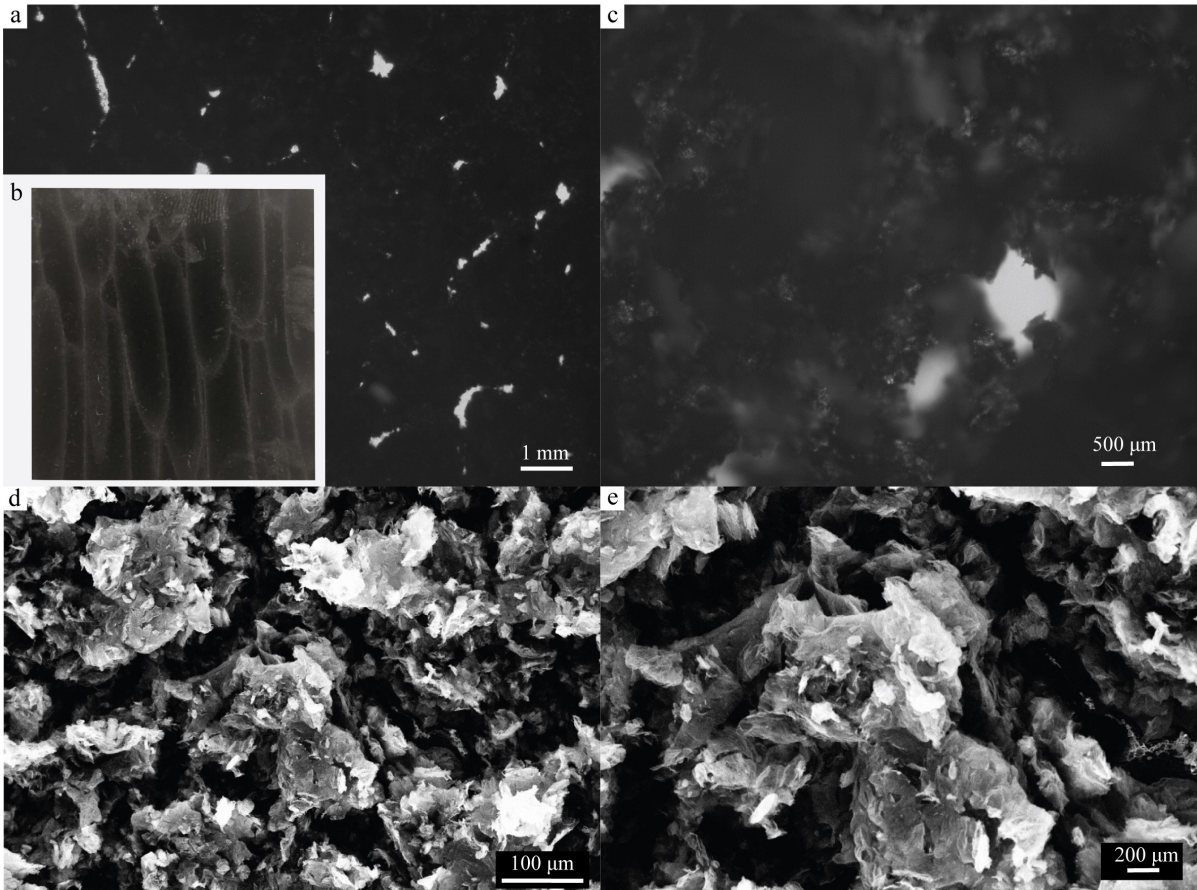


Figure S9. Optical microscopy and SEM images of an RGO layer without micro-cliff patterns (a) optical microscopy image with low magnification. (b) Photo of the sensor captured using a camera. (c) optical microscopy image with high magnification (d) SEM image with 500 \times magnification (e) SEM figure with 1000 \times magnification.

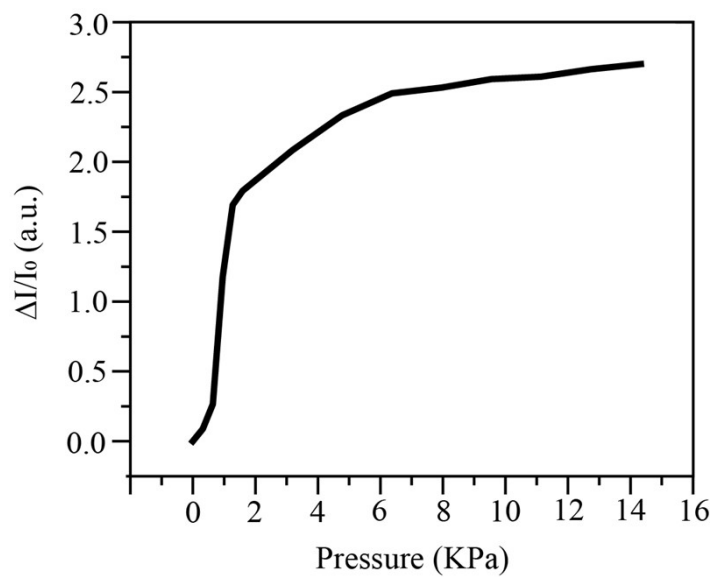


Figure S10. Sensitivity performance of sensor without micro-cliff pattern

8. Filter paper based low detection limit sensor film

A graphene micro-cliff pressure sensor that uses filter paper (Polyethersulfone membrane) as substrate has been made to achieve low detection limit, as shown in **Figure S11**. The graphene oxide film is coated on the filter paper using filtration method and then reduced by a flash with a mask.

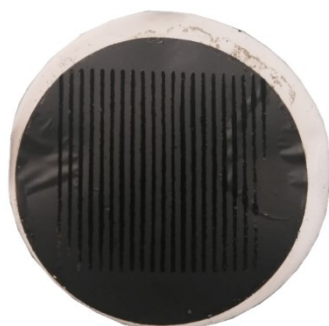


Figure S11. Micro-cliff pressure-sensing layer using filter paper as the substrate.

9. Sensitivity performance of our work and comparison of performance to similar work in recent articles

Table S1 shows the performance of the micro-cliff sensor benchmarked against the representative state-of-the-art piezoresistive pressure sensors ^[4-12]

Active Materials	Working Range	Sensitivity	Response/Recover Time (ms)	Stability	Reference
Micro-cliff RGO film	0.3 - 255 KPa	72568 KPa^{-1} (0.32 - 3.2 KPa), 43615 KPa^{-1} (0.32 - 11.5 KPa), 938 KPa^{-1} (48 - 160 KPa)	5/3	5000	This Work
Laser Induced Graphene/PS	< 100 KPa	149 KPa^{-1} (< 1 KPa), 659 KPa^{-1} (1-10 KPa), 2048 KPa^{-1} (10 - 100 KPa)	16 /27	1000	4

polypyrrole/PDMS micropylramid	< 1 KPa	1907.2 KPa^{-1} (< 100 Pa), 461.5 KPa^{-1} (< 1 KPa)	0.05/6.2	15000	5
PEDOT:PSS/PDMS	< 20 KPa	851 KPa^{-1} (< 3 KPa)	0.15	20000	6
Continuous-gradient Wrinkles RGO	42Pa - 3 KPa	78.5 KPa^{-1} (100 – 200 Pa)	261/131	1200	7
DNTT/PDMS/Au	< 90 KPa	514 KPa^{-1} (< 250 Pa)	1.8/6.7	10000	8
MXene Sphere/Reduced Graphene Aerogel Composites	< 10 KPa	609 KPa^{-1} (6.4 Kpa – 10 KPa)	232/225	6000	9
MXene/PVA NWs	< 20 KPa	442 KPa^{-1} (5.37 KPa – 18.56 KPa)	138/127	10000	10
SnSe_2 Nanoplates/PDMS/Au	< 38.4 KPa	433.22 KPa^{-1} (< 2.91 KPa)	0.07/0.09	4000	11
self-assembled Graphene	< 40 KPa	1875.5 KPa^{-1} (< 20KPa), 853.2 KPa^{-1} (> 20 KPa)	0.5/0.8	15000	12

Abbreviations: RGO, reduced graphene oxide;PS, Polystyrene;PDMS, Polydimethylsiloxane; PEDOT:PSS, poly(3,4-ethylenedioxythiophene) polystyrene sulfonate;DNTT, dinaphtho[2,3-b:2',3'-f]thieno[3,2-b]thiophene;Au, Aurum; PVA, Polyvinyl Alcohol; NWs, nanowires

10. Absolute resistance value of the sensor under different pressures

The measured absolute resistance value of the sensor under different pressures is shown in

Figure S12.

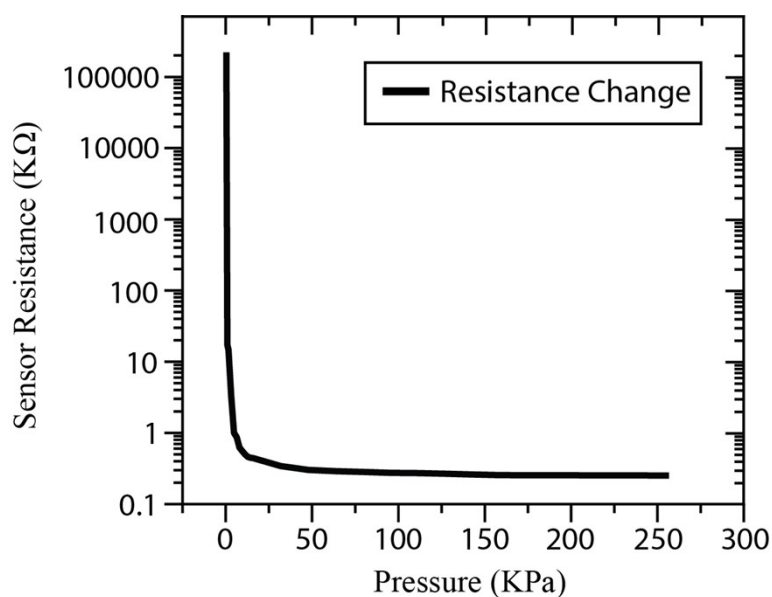


Figure S12. Absolute resistance value of the sensor under different pressures.

Reference

1. Cost, J. R.; Janowski, K. R.; Rossi, R. C., Elastic properties of isotropic graphite. *The Philosophical Magazine: A Journal of Theoretical Experimental and Applied Physics* **1968**, *17* (148), 851-854.
2. Teklu, A.; Barry, C.; Palumbo, M.; Weiwadel, C.; Kuthirummal, N.; Flagg, J., Mechanical Characterization of Reduced Graphene Oxide Using AFM. *Advances in Condensed Matter Physics* **2019**, *2019*, 8713965.
3. Niu, Y.; Zhao, J.; Zhang, X.; Wang, X.; Wu, J.; Li, Y.; Li, Y., Large area orientation films based on graphene oxide self-assembly and low-temperature thermal reduction. *Applied Physics Letters* **2012**, *101* (18), 181903.
4. Tian, Q.; Yan, W.; Li, Y.; Ho, D., Bean Pod-inspired Ultra-sensitive and Self-healing Pressure Sensor Based on Laser Induced Graphene and Polystyrene Microspheres Sandwiched Structure. *ACS Applied Materials & Interfaces* **2020**.
5. Li, H.; Wu, K.; Xu, Z.; Wang, Z.; Meng, Y.; Li, L., Ultrahigh-Sensitivity Piezoresistive Pressure Sensors for Detection of Tiny Pressure. *ACS Applied Materials & Interfaces* **2018**, *10* (24), 20826-20834.
6. Wang, Z.; Wang, S.; Zeng, J.; Ren, X.; Chee, A. J. Y.; Yiu, B. Y. S.; Chung, W. C.; Yang, Y.; Yu, A. C. H.; Roberts, R. C.; Tsang, A. C. O.; Chow, K. W.; Chan, P. K. L., High Sensitivity, Wearable, Piezoresistive Pressure Sensors Based on Irregular Microhump Structures and Its Applications in Body Motion Sensing. *Small* **2016**, *12* (28), 3827-3836.
7. Jia, J.; Huang, G.; Deng, J.; Pan, K., Skin-inspired flexible and high-sensitivity pressure sensors based on rGO films with continuous-gradient wrinkles. *Nanoscale* **2019**.
8. Wang, Z.; Guo, S.; Li, H.; Wang, B.; Sun, Y.; Xu, Z.; Chen, X.; Wu, K.; Zhang, X.; Xing, F.; Li, L.; Hu, W., The Semiconductor/Conductor Interface Piezoresistive Effect in an Organic Transistor for Highly Sensitive Pressure Sensors. *Advanced Materials* **2019**, *31* (6), 1805630.
9. Zhu, M.; Yue, Y.; Cheng, Y.; Zhang, Y.; Su, J.; Long, F.; Jiang, X.; Ma, Y.; Gao, Y., Hollow MXene Sphere/Reduced Graphene Aerogel Composites for Piezoresistive Sensor with Ultra-High Sensitivity. *Advanced Electronic Materials* **2020**, *6* (2), 1901064.

10. Yue, Y.; Liu, N.; Liu, W.; Li, M.; Ma, Y.; Luo, C.; Wang, S.; Rao, J.; Hu, X.; Su, J.; Zhang, Z.; Huang, Q.; Gao, Y., 3D hybrid porous Mxene-sponge network and its application in piezoresistive sensor. *Nano Energy* **2018**, *50*, 79-87.
11. Li, W.; He, K.; Zhang, D.; Li, N.; Hou, Y.; Cheng, G.; Li, W.; Sui, F.; Dai, Y.; Luo, H.; Feng, Y.; Wei, L.; Li, W.; Zhong, G.; Chen, M.; Yang, C., Flexible and High Performance Piezoresistive Pressure Sensors Based on Hierarchical Flower-Shaped SnSe₂ Nanoplates. *ACS Applied Energy Materials* **2019**, *2* (4), 2803-2809.
12. He, J.; Xiao, P.; Lu, W.; Shi, J.; Zhang, L.; Liang, Y.; Pan, C.; Kuo, S.-W.; Chen, T., A Universal high accuracy wearable pulse monitoring system via high sensitivity and large linearity graphene pressure sensor. *Nano Energy* **2019**, *59*, 422-433.